Quasi-two-dimensional Bose-Einstein condensation of spin triplets in the dimerized quantum magnet Ba_{2}CuSi_{2}O_{6}Cl_{2}

Makiko Okada, Hidekazu Tanaka, Nobuyuki Kurita, Kohei Johmoto, Hidehiro Uekusa, Atsushi Miyake, Masashi Tokunaga, Satoshi Nishimoto, Masaaki Nakamura, Marcelo Jaime, Guillaume Radtke, and Andrés Saúl

Quasi-two-dimensional Bose-Einstein condensation of spin triplets in dimerized quantum magnet $Ba_2CuSi_2O_6Cl_2$

Makiko Okada,[1] Hidekazu Tanaka,[1, *] Nobuyuki Kurita,[1] Kohei Johmoto,[2]
Hidehiro Uekusa,[2] Atsushi Miyake,[3] Masashi Tokunaga,[3] Satoshi Nishimoto,[4, 5]
Masaaki Nakamura,[6] Marcelo Jaime,[7] Guillaume Radtke,[8] and Andrés Saúl[9]

[1]*Department of Physics, Tokyo Institute of Technology, Meguro-ku, Tokyo 152-8551, Japan*
[2]*Department of Chemistry, Tokyo Institute of Technology, Meguro-ku, Tokyo 152-8551, Japan*
[3]*Institute for Solid State Physics, University of Tokyo, Kashiwa, Chiba 277-8581, Japan*
[4]*Institute for Theoretical Solid State Physics, IFW Dresden, 01171 Dresden, Germany*
[5]*Department of Physics, Technical University Dresden, 01069 Dresden, Germany*
[6]*Department of Physics, Ehime University, Bunkyo-cho 2-5, Matsuyama, Ehime 790-8577, Japan*
[7]*National High Magnetic Field Laboratory, and Materials, Physics and Applications Division,*
Los Alamos National Laboratory, Los Alamos, NM 87545, USA
[8]*Institut de Minéralogie, de Physique des Matériaux et de Cosmochimie,*
Sorbonne Universités, Université Pierre et Marie Curie - Paris 6, UMR CNRS 7590,
Museum National d'Histoire Naturelle, IRD UMR 206, 75005 Paris, France
[9]*Aix-Marseille University, Centre Interdisciplinaire de Nanoscience de Marseille-CNRS UMR 7325*
Campus de Luminy, 13288 Marseille cedex 9, France
(Dated: August 25, 2016)

We synthesized single crystals of composition $Ba_2CuSi_2O_6Cl_2$ and investigated its quantum magnetic properties. The crystal structure is closely related to that of the quasi-two-dimensional (2D) dimerized magnet $BaCuSi_2O_6$ also known as Han purple. $Ba_2CuSi_2O_6Cl_2$ has a singlet ground state with an excitation gap of $\Delta/k_B = 20.8$ K. The magnetization curves for two different field directions almost perfectly coincide when normalized by the g-factor except for a small jump anomaly for a magnetic field perpendicular to the c axis. The magnetization curve with a nonlinear slope above the critical field is in excellent agreement with exact-diagonalization calculations based on a 2D coupled spin-dimer model. Individual exchange constants are also evaluated using density functional theory (DFT). The DFT results demonstrate a 2D exchange network and weak frustration between interdimer exchange interactions, supported by weak spin-lattice coupling implied from our magnetostriction data. The magnetic-field-induced spin ordering in $Ba_2CuSi_2O_6Cl_2$ is described as the quasi-2D Bose-Einstein condensation of triplets.

PACS numbers: 75.10.Jm, 75.40.Cx, 75.45.+j

I. INTRODUCTION

Bose-Einstein condensation (BEC) is a fascinating macroscopic quantum phenomenon characteristic of system of bosons [1, 2]. BEC occurs not only in true bosonic particles [3–5] but also in bosonic quasiparticles [6, 7]. Dimerized quantum magnets (DQMs) provide a stage to embody the quantum physics of interacting lattice bosons [8, 9]. In a DQM, two spins are dimerized by a strong antiferromagnetic (AFM) exchange interaction and these dimers are coupled via weak exchange interactions. DQMs usually have a gapped singlet ground state and exhibit magnetic-field-induced [10–15] and pressure-induced [16–21] quantum phase transitions (QPTs) to an ordered state. These QPTs can be described as the BEC of the $S_z = \pm 1$ components of the spin triplets called triplons [22–26]. In pressure-induced BEC, the triply degenerate triplons are reconstructed at the quantum critical point (QCP) into one amplitude mode [23],

which can be interpreted as the Higgs mode, and two phase modes, which correspond to the Nambu-Goldstone modes [27]. In magnetic-field-induced BEC of triplons with $S_z = +1$, the particle quantities of chemical potential μ, triplon density n and compressibility $\kappa = \partial n/\partial \mu$ correspond to the magnetic quantities of the external field H, total magnetization M and magnetic susceptibility $\chi = \partial M/\partial H$, respectively, which are easily measured. A feature of triplon BEC is that the total number of triplons is controllable by tuning the magnetic field or pressure, in contrast to the BEC of true particles.

The magnetic-field-induced BEC of triplons in 3D DQMs has been studied experimentally for many systems [10–15], and the results observed were quantitatively or semiquantitatively described by the triplon BEC theory [15, 22, 23]. On the other hand, in 2D systems, long-range ordering is suppressed by large quantum and thermal fluctuations, and topological ordering such as the Berezinskii-Kosterlitz-Thouless (BKT) transition [28–30] and unusual quantum critical behavior are expected to occur. Recently, the BKT transition has been reported for the 2D DQM $C_{36}H_{48}Cu_2F_6N_8O_{12}S_2$ [31]. However, the understanding of 2D systems of interacting triplons is insufficient. For a detailed study of the

*Electronic address: tanaka@lee.phys.titech.ac.jp

systems, a new 2D-like DQM, for which sizable single crystals are obtainable, is necessary. In this paper, we show that $Ba_2CuSi_2O_6Cl_2$, synthesized in this work, is close to an ideal 2D dimerized isotropic quantum magnet, which exhibits field-induced magnetic order in laboratory-accessible critical fields.

II. EXPERIMENTAL DETAILS

To synthesize single crystals of $Ba_2CuSi_2O_6Cl_2$, we first prepared Ba_2CuTeO_6 powder by a solid-state reaction. A mixture of Ba_2CuTeO_6 and $BaCl_2$ in a molar ratio of $1:10$ was vacuum-sealed in a quartz tube. The temperature at the center of the horizontal tube furnace was lowered from 1100 to 800°C over 10 days. Plate-shaped blue single crystals with a maximum size of $3 \times 3 \times 1$ mm^3 were obtained. These crystals were found to be $Ba_2CuSi_2O_6Cl_2$ from X-ray diffraction, where the silicon was provided by the quartz tube. The wide plane of the crystals was confirmed to be the crystallographic ab plane by X-ray diffraction. We found that the quartz tube frequently exploded during cooling to room temperature after the crystallization process from 1100 to 800°C. To avoid hazardous conditions and damage to the furnace, a cylindrical nichrome protector was inserted in the furnace core tube.

The magnetic susceptibility of $Ba_2CuSi_2O_6Cl_2$ single crystal was measured in the temperature range of $1.8 - 300$ K using a SQUID magnetometer (Quantum Design MPMS XL). The specific heat of $Ba_2CuSi_2O_6Cl_2$ was measured in the temperature range of $0.5 - 300$ K using a physical property measurement system (Quantum Design PPMS) by the relaxation method. High-field magnetization measurement in a magnetic field of up to 45 T was performed at 4.2 and 1.4 K using an induction method with a multilayer pulse magnet at the Institute for Solid State Physics, University of Tokyo.

Magnetostriction of $Ba_2CuSi_2O_6Cl_2$ was measured at National High Magnetic Field Laboratory, Los Alamos National Laboratory. Variations in the sample length L as a function of the temperature and/or magnetic field, $\varepsilon(H) = \Delta L/L(H) = [L(H,T) - L(H_0,T_0)]/L(H_0,T_0)$, were measured using a fiber Bragg grating (FBG) technique [32, 33] consisting of recording spectral information of the light reflected by a 0.5-mm-long Bragg grating inscribed in the core of a 125 μm telecom optical fiber. The FBG section of the fiber is attached to the sample to be studied, and changes in the grating spacing are driven by changes in the sample dimensions when the temperature or magnetic field is changed. This technique has a demonstrated resolution of $\Delta L/L \simeq 10^{-7}$ that is virtually immune to the electromagnetic noise characteristic of pulsed magnetic fields but is somewhat sensitive to mechanical vibrations. Capacitor-bank-driven pulsed magnets were used to produce 25 ms magnetic field pulses up to 60 T.

TABLE I: Crystal data for $Ba_2CuSi_2O_6Cl_2$.

Chemical formula	$Ba_2CuSi_2O_6Cl_2$
Space group	$Cmca$
a (Å)	13.8917(12)
b (Å)	13.8563(11)
c (Å)	119.6035(15)
V (Å^3)	3773.4(5)
Z	16
R; wR	0.0773; 0.1638

TABLE II: Fractional atomic coordinates $(\times 10^4)$ and equivalent isotropic displacement parameters $(\text{Å}^2 \times 10^3)$ for $Ba_2CuSi_2O_6Cl_2$.

Atom	x	y	z	U_{eq}
Ba(1)	2715(1)	6230(1)	1093(1)	25(1)
Ba(2)	0	3917(1)	1045(1)	24(1)
Ba(3)	5000	3535(1)	1046(1)	27(1)
Cl(1)	2512(5)	3562(3)	429(3)	51(2)
Cl(2)	0	1390(9)	569(4)	68(3)
Cl(3)	5000	1244(6)	585(5)	74(3)
Cu(1)	2503(1)	3783(2)	1761(1)	17(1)
O(1)	1747(8)	4919(9)	1819(7)	24(3)
O(2)	3693(9)	4495(8)	1820(7)	26(3)
O(3)	1231(8)	6241(8)	2728(6)	21(2)
O(4)	0	4941(12)	2251(9)	22(4)
O(5)	3278(8)	2565(8)	1827(6)	20(2)
O(6)	0	2532(11)	2750(8)	19(3)
O(7)	1334(8)	2960(8)	1822(6)	20(2)
Si(1)	1111(4)	5122(3)	2495(3)	21(1)
Si(2)	1109(4)	2376(3)	2499(2)	15(1)

III. COMPUTATIONAL DETAILS

Band structure and total energy calculations were performed with the QUANTUM ESPRESSO [34] suite of codes based on density functional theory (DFT) and using the pseudopotential plane-wave method. The calculations were performed using ultrasoft pseudopotentials [35] with plane-wave and charge density cutoffs of 60 Ry and 400 Ry, respectively, and a $4 \times 4 \times 2$ Monkhorst-Pack [36] grid for the first Brillouin zone sampling of the 104-atom base-centered orthorhombic unit cell of $Ba_2CuSi_2O_6Cl_2$.

Exchange and correlation were taken into account using the generalized gradient approximation of Perdew, Burke and Ernzerhof [37] (GGA-PBE) augmented by a Hubbard U term to improve the treatment of strongly correlated Cu-3d electrons. A value of $U_{scf} = 10.4$ eV for the effective self-consistent Hubbard term was determined for the 104-atom unit cell following the approach described in Refs. [38] and [39], using the experimental structure determined at 300 K and a ferromagnetic order.
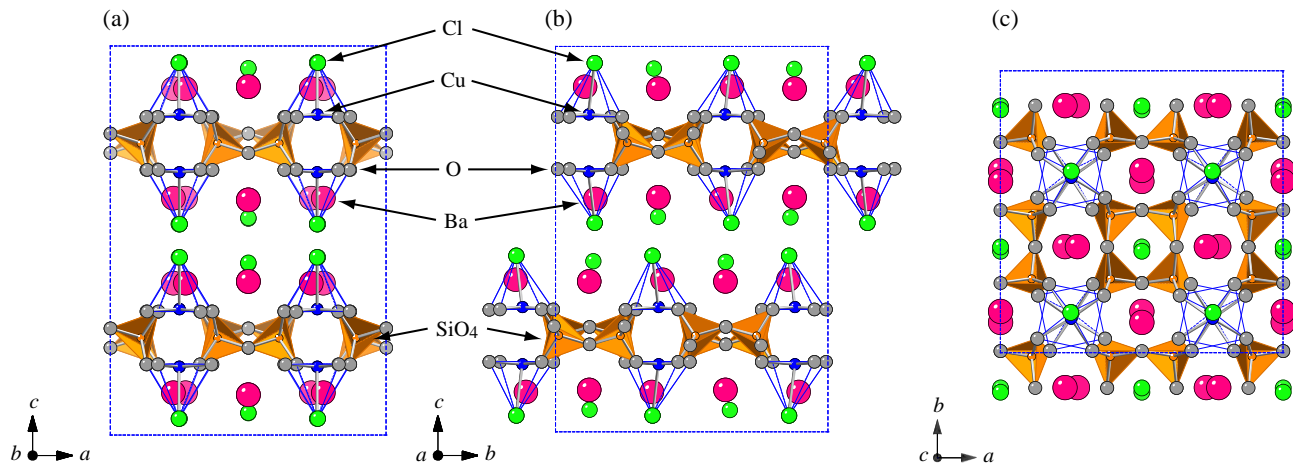
FIG. 1: (Color online) Crystal structure of $Ba_2CuSi_2O_6Cl_2$ viewed along the (a) b axis, (b) a axis and (c) c axis.

Maximally localized Wannier function [40] (MLWF) interpolation of the band structure was performed using WANNIER90 [41], which allows the extraction of effective hopping integrals between magnetic orbitals.

The calculation of magnetic couplings was carried out within the broken symmetry formalism, *i.e.*, by mapping total energies corresponding to various collinear spin arrangements within a supercell [42] onto the Heisenberg Hamiltonian

$$\mathcal{H} = \mathcal{H}_0 + \sum_{\langle i,j \rangle} J_{ij}\, \boldsymbol{S}_i \cdot \boldsymbol{S}_j, \qquad (1)$$

where $\mathcal{H}_0$ is the spin-independent part of the Hamiltonian, J_{ij} are the magnetic couplings to be determined, and $\boldsymbol{S}_i$ and $\boldsymbol{S}_j$ are, in our case, the $S, = 1/2$ spin operators localized on Cu^{2+} ions located at sites i and j respectively. It is straightforward to show that the expectation value of the Hamiltonian (1) on a DFT state $|\alpha\rangle$ (obtained by preparing the initial electron density according to a particular collinear spin arrangement in the supercell and performing a self-consistent calculation until convergence) can be simply written in the form of the Ising Hamiltonian [43]

$$\epsilon_\alpha^{\mathrm{DFT}} = \langle \alpha|\mathcal{H}|\alpha\rangle = \epsilon_0 + \frac{1}{4}\sum_{\langle i,j \rangle} J_{ij}\sigma_i\sigma_j \qquad (2)$$

with $\sigma_i = \pm 1$. In strongly localized systems, such as $3d$ transition-metal oxides, Eq. (2) can be employed to model large sets of spin configurations, and a least-squares minimization of the difference between the DFT and Ising relative energies can be applied to obtain a numerical evaluation of the couplings [44, 45].

IV. CRYSTAL STRUCTURE

We performed a structural analysis at room temperature using a RIGAKU R-AXIS RAPID three-circle X-ray diffractometer equipped with an imaging plate area detector. Monochromatic Mo-Kα radiation with a wavelength of $\lambda = 0.71075$ Å was used as the X-ray source. Data integration and global-cell refinements were performed using data in the range of $3.119° < \theta < 27.485°$, and absorption correction based on face indexing and integration on a Gaussian grid was also performed. The total number of reflections observed was 17599, among which 2252 reflections were found to be independent and 1521 reflections were determined to satisfy the criterion $I > 2\sigma(I)$. Structural parameters were refined by the full-matrix least-squares method using SHELXL−97 software. The final R indices obtained for $I > 2\sigma(I)$ were $R = 0.0773$ and $wR = 0.1638$. The crystal data are listed in Table I. The chemical formula was confirmed to be $Ba_2CuSi_2O_6Cl_2$ (BCuSOC). The structure of BCuSOC is orthorhombic $Cmca$ with cell dimensions of $a = 13.8917(12)$ Å, $b = 13.8563(11)$ Å, $c = 19.6035(15)$ Å and $Z = 16$. Its atomic coordinates and equivalent isotropic displacement parameters are shown in Table II.

The structure of BCuSOC, closely related to that of $Ba_2CoSi_2O_6Cl_2$ [46], is orthorhombic $Cmca$ with cell dimensions of $a = 13.8917(12)$ Å, $b = 13.8563(11)$ Å and $c = 19.6035(15)$ Å. The crystal structure viewed along the b, a and c axes is illustrated in Figs. 1(a), (b) and (c), respectively. The crystal structure comprises CuO_4Cl pyramids with a Cl^- ion at the apex. Magnetic Cu^{2+} with spin-1/2 is located approximately at the center of the base composed of O^{2-}, which is parallel to the ab plane. Two neighboring CuO_4Cl pyramids along the c axis are placed with their bases facing each other. The CuO_4Cl pyramids are linked via SiO_4 tetrahedra in the ab plane, as shown in Fig. 1(c). The atomic linkage in the ab plane is approximately the same as that of $BaCuSi_2O_6$ [47–49]. Two bases of neighboring CuO_4Cl pyramids are rotated in opposite directions around the c axis, as observed in $BaCuSi_2O_6$. Such rotation of the bases of the CoO_4Cl pyramids is absent in $Ba_2CoSi_2O_6Cl_2$ [46].

V.   RESULTS AND ANALYSES

Figure 2(a) shows the temperature dependence of the magnetic susceptibilities $\chi(T)$ for BCuSOC with $H \parallel c$ and $H \perp c$. The susceptibility data are normalized by the g-factors of $g_\parallel = 2.32$ and $g_\perp = 2.06$, determined from electron paramagnetic resonance data at room temperature. The normalized susceptibilities $(2/g)^2 \chi(T)$ almost perfectly coincide above 6 K, which indicates that the anisotropy of the magnetic interactions is very small. The susceptibility has a rounded maximum at $T_{\max} \simeq 18$ K, followed by a rapid decrease with decreasing temperature. No anomaly indicative of a phase transition was observed down to the lowest temperature of 1.8 K. The upturn in $\chi(T)$ below 4 K is likely due to unpaired spins produced by lattice defects. The overall feature of $\chi(T)$ is characteristic of Heisenberg spin dimer magnets with a gapped singlet ground state.
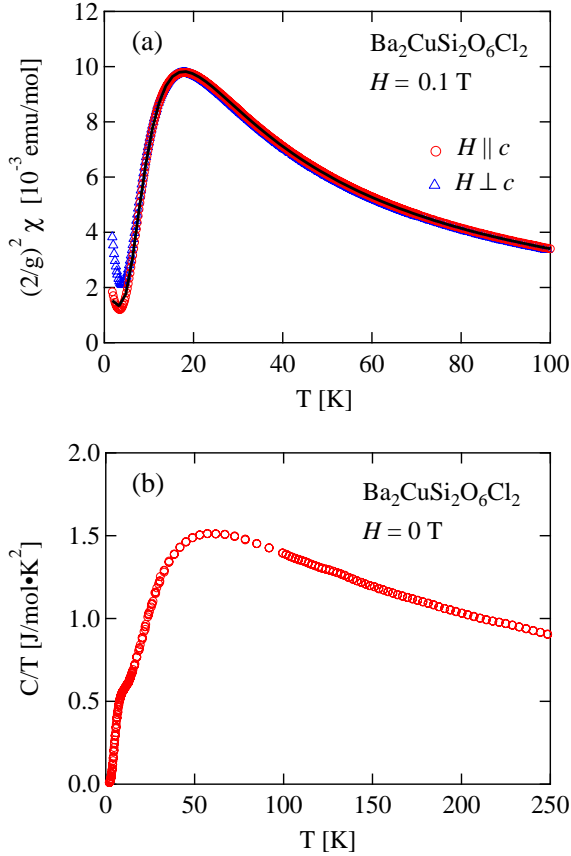

FIG. 2: (Color online) (a) Temperature dependence of magnetic susceptibilities of BCuSOC measured for $H \parallel c$ and $H \perp c$, which are normalized by the g-factors of $g_\parallel = 2.32$ and $g_\perp = 2.06$. The solid line denotes the fit obtained using Eq. (3). (b) Temperature dependence of total specific heat divided by the temperature measured at zero magnetic field.

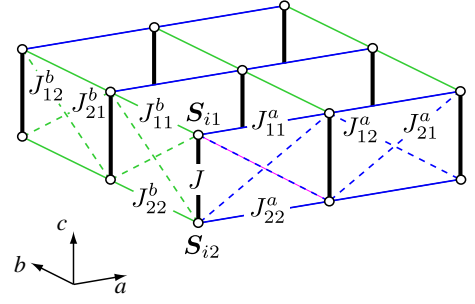It is natural to assume that the two Cu^{2+} spins located on the bases of neighboring CuO_4Cl pyramids along the

FIG. 3: (Color online) 2D model of the exchange network in $Ba_2CuSi_2O_6Cl_2$. Thick solid lines represent the intradimer exchange interaction J, and thin solid and dashed lines respectively represent the interdimer exchange interactions $J^a_{\alpha\beta}$ and $J^b_{\alpha\beta}$ ($\alpha, \beta = 1, 2$).

c axis are coupled to form an AFM dimer. Because magnetic excitation in $BaCuSi_2O_6$ is dispersive in the ab plane and dispersionless along the c direction [49], BCuSOC can approximate a 2D coupled spin dimer system with the exchange network shown in Fig. 3. This is confirmed by the DFT calculation shown later. Because the crystal structure is nearly tetragonal, we can assume that $J^a_{11} = J^a_{22} = J^b_{11} = J^b_{22} \equiv J_p$ and $J^a_{12} = J^a_{21} = J^b_{12} = J^b_{21} \equiv J_d$.

When interdimer exchange interactions are treated as mean fields, the magnetic susceptibility is expressed by

$$\chi(T) = \frac{g^2 \mu_B^2 \beta N}{\exp(\beta J) + 3 + \beta J'}, \tag{3}$$

where $\beta = 1/(k_B T)$, N is the number of spins, J is the intradimer exchange interaction and J' is the sum of the interdimer interactions acting on one spin in a dimer, which is given for the present system by $J' = 4(J_p + J_d)$. Fitting Eq. (3) with the Curie and constant terms to the experimental susceptibility for $H \parallel c$, we evaluate J and J' as $J/k_B = 29.4$ K and $J'/k_B = 13.8$ K, which are consistent with $J/k_B = 28.1$ K and $J'/k_B = 17.2$ K evaluated from the analysis of the magnetization curve, shown below. The solid line in Fig. 2(a) denotes the fit, which excellently reproduces the experimental susceptibility.

Figure 2(b) shows the total specific heat divided by the temperature of BCuSOC measured at zero magnetic field. No anomaly indicative of a structural phase transition was observed down to 0.5 K, although in $BaCuSi_2O_6$, a structural phase transition was observed at $T_s \simeq 100$ K [50]. In $BaCuSi_2O_6$, there are three types of dimer with different exchange interactions J below T_s [51]. The absence of the structural phase transition in BCuSOC indicates that all the dimers are likely magnetically equivalent down to 0.5 K. A Schottky-like anomaly is observed around 10 K owing to the excitation gap of $\Delta/k_B = 20.8$ K, which is determined through the high-magnetic-field magnetization measurement described below.

Figure 4(a) shows the magnetization curves of BCuSOC and their field derivatives measured at 1.4 K for $H \parallel c$ and $H \perp c$ upon sweeping the magnetic field up-
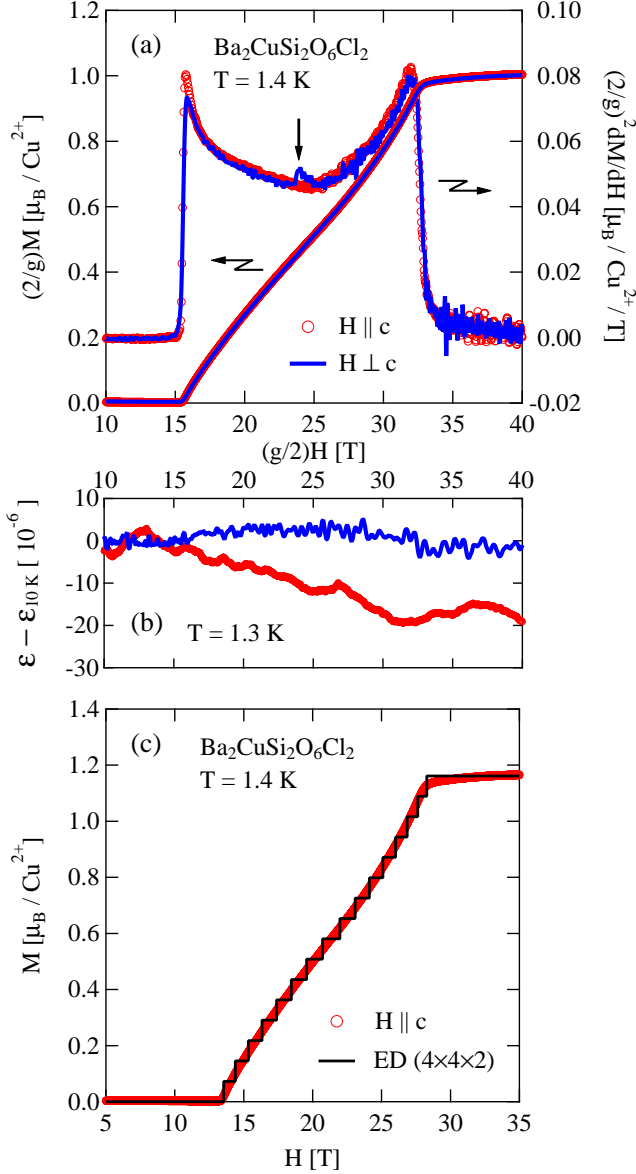
FIG. 4: (Color online) (a) Magnetic-field dependence of magnetization M and its field derivative dM/dH for BCuSOC measured at 1.4 K for $H \parallel c$ and $H \perp c$, which are normalized by the g-factors. An arrow indicates an anomaly in dM/dH for $H \perp c$ owing to a phase transition accompanied with a small magnetization jump. (b) Axial magnetostriction $\varepsilon_a(H)$, with $H \perp c$ and $H \parallel c$, at $T = 1.3$ K after subtraction of the smooth background of similar magnitude measured at $T = 10$ K. The magnetostriction along and perpendicular to the c axis (at $(g/2)H = 25$ T) show magnitudes and signs which, in a magnetically isotropic system, would indicate conservation of the unit cell volume. (c) Comparison between experimental and theoretical magnetization curves for $H \parallel c$. The theoretical result was obtained using exact diagonalization (ED) for a 32-site spin cluster.

respective g-factors. The measurement was performed up to a magnetic field of 45 T using an induction method with a multilayer pulse magnet at the Institute for Solid State Physics, University of Tokyo. The entire magnetization process was observed within the experimental field range.

The magnetization curves and their field derivatives for $H \parallel c$ and $H \perp c$ almost perfectly coincide, except for a small jump indicated by the vertical arrow in Fig. 4(a). These results confirm, as for $\chi(T)$ discussed before, that the anisotropy in the spin-spin interactions is very small. The critical field H_c and saturation field H_s are determined to be $(g/2)H_c = 15.5$ T and $(g/2)H_s = 32.8$ T. From H_c, the excitation gap is evaluated to be $\Delta/k_B = 20.8$ K. Note that $H_s/H_c = 2.12$ for BCuSOC is almost the same as $H_s/H_c = 2.1$ in BaCuSi$_2$O$_6$, where $H_c = 23.5$ T and $H_s = 49$ T for $H \parallel c$ [13]. For BCuSOC, the magnetization curve for $H_c < H < H_s$ is "inverse S" shaped, which is characteristic of a low-dimensional quantum antiferromagnet. The linear magnetization slope observed in BaCuSi$_2$O$_6$ [13] is likely a consequence of having three types of dimer.

The axial magnetostriction $\varepsilon_a = (L(H) - L(0))/L(0)$ for $H \parallel c$ and $H \perp c$ was measured at 1.3 K up to 45 T and is shown in Fig. 4(b) after subtraction of the smooth background obtained at $T = 10$ K. $\varepsilon_a(H)$ shows a lattice response $\Delta L/L$ in the 10^{-5} range for both orientations in the middle of the field-induced magnetically ordered state in BCuSOC, i.e., at $(g/2)H = 25$ T. The observed magnitude is rather small for an insulator and similar to or smaller than values observed for other BEC systems where geometrical frustration is weak. Indeed, the magnetostriction in the archetypical system NiCl$_2$-4SC(NH$_2$)$_2$ was also found to be in the 10^{-4} to 10^{-5} range [52]. Here, the lattice response to an applied field was used to quantify spin-spin correlations which, in combination with the measured Young's modulus, were instrumental in computing the dependence of the superexchange constant J on the Ni interionic distance z, dJ/dz. While similar computations for BCuSOC are beyond the scope of this letter, it is a topic worth exploring in future research [52].

Because the spin dimers are parallel to the c axis and the magnetization shows no anomaly between H_c and H_s for $H \parallel c$, we infer that $U(1)$ symmetry with respect to the c axis exists in BCuSOC. We analyzed the magnetization process for $H \parallel c$ using exact diagonalization (ED) calculation for a 32-site ($4 \times 4 \times 2$) spin cluster on the basis of the exchange model shown in Fig. 1(d). Varying the exchange parameters, we compared the calculated results with the experimental magnetization curve. The best fit was obtained with $J/k_B = 28.1$ K, $J_p/k_B = 3.9$ K and $J_d/k_B = 0.4$ K or with $J_p/k_B = 0.4$ K and $J_d/k_B = 3.9$ K. The solid line in Fig. 4(c) is the magnetization curve calculated with these exchange parameters. The agreement between the experimental and theoretical magnetization curves is excellent. The present results demonstrate that BCuSOC closely approximates the 2D coupled Heisen-
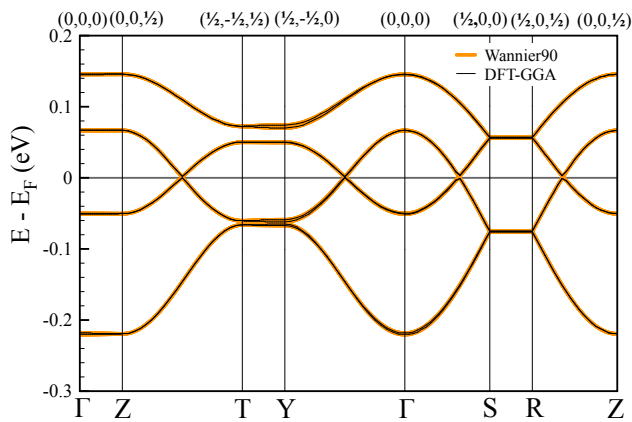
ward. The magnetization data were normalized by the

FIG. 5: (color online) Detail of the Cu-$3d_{x^2-y^2}$ band manifold around the Fermi level in $Ba_2CuSi_2O_6Cl_2$ calculated using paramagnetic GGA-PBE and interpolated with MLWFs.

berg spin dimer system. Within the ED calculation, we cannot determine whether the parallel J_p or diagonal J_d interdimer interaction is dominant. This point will be addressed below using DFT calculations.

For $H \perp c$, $M(H)$ shows a small jump at $M \simeq 0.5M_s$, which is evident in dM/dH (Fig. 4(a)). The magnetization anomaly observed upon sweeping the magnetic field upward and downward is intrinsic. It is considered that the magnetization jump arises from spin reorientation. Because the inversion symmetry with respect to the midpoint of the two spins in a dimer is absent, the Dzyaloshinskii-Moriya (DM) interaction of the form $D_i \cdot [S_{i1} \times S_{i2}]$ between spins S_{i1} and S_{i2} [53, 54] can be finite, although it is small. The D vector must be in the ac plane because of the twofold axis passing through the midpoint of the dimer along the b axis [54]. The magnetization curve for $H \parallel c$ shows no anomaly, hence the a axis component of the D vector will be small. The c axis components of the D vectors on the neighboring dimers should be antiparallel dueowing to the mirror plane at $a/2$ and the glide planes at $\pm c/4$. The DM interaction is usually accompanied with anisotropy of the form $(S_{i1} \cdot D_i)(S_{i2} \cdot D_i)/(2J)$ (known as the KSEA interaction) [55–57]. The KSEA interaction favors spins parallel to the D vector, which is assumed to be parallel to the c axis, while the DM interaction favors spins perpendicular to the c axis. Thus, competition between the DM and KSEA interactions occurs, likely giving rise to a spin reorientation transition for $H \perp c$.

VI.   DENSITY FUNCTIONAL CALCULATIONS

To assess the validity of our discussion on the basis of a microscopic analysis, isotropic magnetic couplings were estimated using DFT calculations [34, 35]. As the first step, Wannier function interpolation [41] of the GGA-PBE [37] paramagnetic bands of the dominant Cu-$3d_{x^2-y^2}$ character was carried out. The results are shown in Figure 5. The corresponding hopping integrals are summarized in Table III. An estimate of the AFM contribution to the magnetic couplings can indeed be achieved through mapping of the paramagnetic band structure onto a single-band Hubbard model at half filling, eventually reducing to an AFM Heisenberg model in the strongly correlated limit. In this approach, the effective interaction is given by $J_{\alpha\beta}^{AFM} = 4t_{\alpha\beta}^2/U_{eff}$. It can be readily seen from Table III that the largest hopping integral (t) occurs between two Cu^{2+} ions located within the same structural dimer, revealing the potential presence of a leading nearest-neighbor AFM coupling. The next largest interactions ($t_{12}^a = t_{21}^a \approx t_{12}^b = t_{21}^b \equiv t_d$) couple two Cu^{2+} ions belonging to one of the four neighboring dimers but located in adjacent planes of the same bilayer. The remaining interactions within the bilayer ($t_{11}^a = t_{22}^a \approx t_{11}^b \approx t_{22}^b \equiv t_p$) are an order of magnitude smaller, and inter-bilayer interactions ($t_\perp$ and $t'_\perp$) are vanishingly weak. This hierarchy in the order of magnitude can easily be seen in Figure 5 using a simple 2D tight-binding analysis. The use of a 2D model is justified by the absence of a sizable dispersion along $\Gamma \to Z$ or $S \to R$, and therefore, the absence of sizable inter-bilayer interactions. Neglecting the inter-bilayer interactions $t_\perp$ and $t'_\perp$, the Cu-$3d_{x^2-y^2}$ band energy dispersions are given by

$$\left.\begin{aligned}
\epsilon_{a,\pm}(\mathbf{k}) = \epsilon_d + t \pm 4(t_p + t_d)\cos(\pi k_x)\cos(\pi k_y), \\
\epsilon_{b,\pm}(\mathbf{k}) = \epsilon_d - t \pm 4(t_p - t_d)\cos(\pi k_x)\cos(\pi k_y),
\end{aligned}\right\} \quad (4)$$

where t_p is the interdimer hopping parallel to the ab plane, t_d is the diagonal interdimer hopping and $\mathbf{k} = (k_x, k_y)$ is the 2D reciprocal vector in units of the reciprocal lattice basis vectors. These two groups of bands are shifted with respect to each other by twice the intradimer hopping t, whose value can readily be determined at S, or to a lesser extent because of additional splittings occurring under the effect of further couplings at T or Y. The band dispersion, as observed along $\Gamma \to S$ for instance, is directly related to the interdimer interaction t_d either through ($t_p + t_d$) for the lower-energy group of bands or through ($t_p - t_d$) for the higher-energy group.

These results provide a clear picture of the dominant AFM magnetic couplings in $Ba_2CuSi_2O_6Cl_2$: the largest interaction J^{AFM} arises within the structural dimers, which are then coupled together by a weaker interdimer interaction J_d^{AFM}. Their ratio can be estimated to be $J_d^{AFM}/J^{AFM} = (t_d/t)^2 \approx 0.22$. Other interactions, arising either within the bilayers or between them, exhibit a negligible AFM component.

Figure 6 shows the MLWF corresponding to the band interpolation presented in Fig. 5. Its dominant Cu-$3d_{x^2-y^2}$ character is clearly apparent, as well as the large antibonding tails held by the four coordinating oxygen atoms O1, O2, O5 and O7. Note however, that non-negligible components are also visible on

TABLE III: Magnetic couplings in $Ba_2CuSi_2O_6Cl_2$: Cu-Cu distances d [Å], hopping integrals t [meV] and magnetic couplings J calculated using GGA+U_{scf} [K]. Hopping integrals are related to the AFM component of the couplings through the relation $J_{\alpha\beta}^{AFM} = 4t_{\alpha\beta}^2/U_{eff}$ where U_{eff} is the effective Hubbard repulsion term. Positive couplings imply AFM interactions.

	t	t_{11}^a	t_{22}^a	t_{11}^b	t_{22}^b	t_{12}^a	t_{21}^a	t_{12}^b	t_{21}^b	$t_\perp$	$t'_\perp$
d (in Å)	2.90	6.95	6.94	6.93	6.93	7.53	7.53	7.51	7.51	7.68	7.77
t (in meV)	-64	5	8	5	5	28	28	32	32	0	0

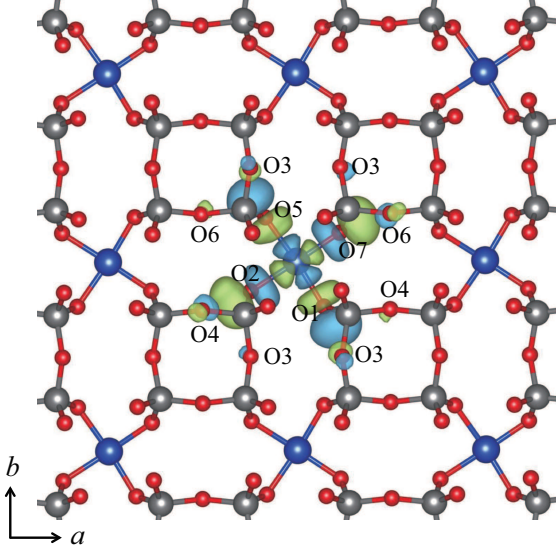|	J	J_p				J_d				$J_\perp$	
J (in K)	30.5	-0.2				5.9				-0.3	

FIG. 6: (color online) MLWF centered on a Cu site. Large antibonding O-2p tails are clearly visible on the Cu coordinating oxygen atoms.
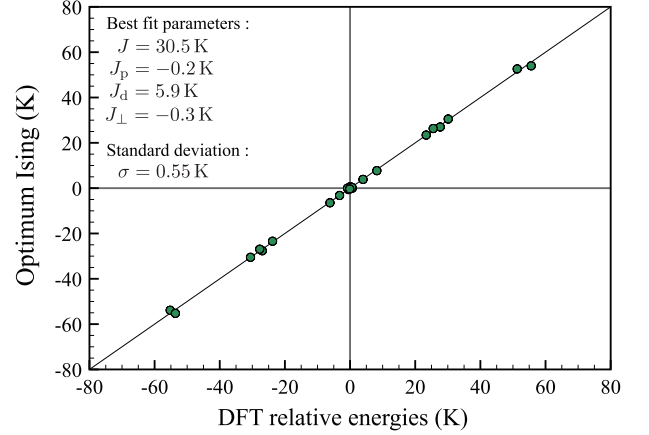

FIG. 7: (color online) Graphical representation of the results obtained by the least-squares fitting procedure employed to evaluate the magnetic couplings: optimized energies calculated with the Ising Hamiltonian (2) are represented as a function of the DFT + U_{scf} relative energies. Positive couplings correspond to AFM interactions according to Eq. (1).

the oxygen atoms bridging two nonmagnetic [SiO$_4$]$^{4-}$ units, i.e. O3, O4 and O6. As already discussed by Mazurenko *et al.* for BaCuSi$_2$O$_6$ [58], the larger interdimer coupling J_d ($J_{12} = J_{21}$) occurs between Cu^{2+} ions belonging to adjacent layers and involves three oxygen atoms. This essentially follows from the larger orbital overlap along paths such as Cu−O5−O6−O7−Cu and Cu−O1−O4−O2−Cu along a or Cu−O2−O3−O4−Cu and Cu−O1−O3−O5−Cu along b associated with larger $\widehat{O-O-O}$ angles ($\approx 150-151°$) than those involved in the same type of path for J_p ($J_{11} \approx J_{22}$), i.e., between Cu^{2+} ions of adjacent dimers belonging to the same atomic layer (from ≈ 87 to $141°$).

Alternatively, magnetic couplings were evaluated by energy differences using the total energies calculated by GGA+U_{scf} for 22 distinct spin configurations obtained in the 104-atom base-centred orthorhombic unit cell. DFT relative energies are shown in Fig. 7 as a function of their optimal Ising counterparts for the simplified model represented in Figure 3. The excellent fit obtained for the entire set of spin configurations fur-

ther justifies the suitability of the simplified Heisenberg Hamiltonian for modeling the magnetic properties of Ba$_2$CuSi$_2$O$_6$Cl$_2$. Their values are presented in Table III. These calculations confirm that the dominant magnetic coupling is AFM, $J/k_B = 30.5$ K, and that it occurs within structural dimers coupled antiferromagnetically through a weaker interaction, $J_d/k_B = 5.9$ K. Note that the amplitude ratio between the interdimer and intradimer couplings, $J_d/J \approx 0.19$, is in close agreement with the value deduced from the analysis of the paramagnetic band structure (≈ 0.22) but slightly overestimates the ratio deduced from the analysis of the magnetization curves (≈ 0.13). The remaining couplings are very weak and ferromagnetic (FM). The overall microscopic picture of the magnetism in Ba$_2$CuSi$_2$O$_6$Cl$_2$ provided by density functional calculations is therefore very similar to that of BaCuSi$_2$O$_6$ [58], where interdimer coupling J_d connects spins belonging to distinct atomic planes forming the bilayer. Furthermore, the presence of weak FM couplings between adjacent spins belonging to the same atomic plane or between the bilayers implies the absence of obvious frustration, in contrast to the case of

$Ba_2CoSi_2O_6Cl_2$ [46].

VII. CONCLUSION

In conclusion, we have presented the first structural analysis, magnetization and magnetoelastic measurements on $Ba_2CuSi_2O_6Cl_2$. The magnetic susceptibilities and magnetization curves for different field directions coincide almost perfectly when normalized by the respective g-factors, which indicates that the magnetic anisotropy is very small. The observed magnetization data are excellently reproduced using exact-diagonalization computations based on the 2D coupled dimer model illustrated in Fig. 1(d). The 2D exchange model was also confirmed by DFT. Thus, $Ba_2CuSi_2O_6Cl_2$ closely approximates the ideal 2D dimerized Heisenberg quantum magnet. The quantum critical behavior near both critical fields $H_{c,s}$ and the nature of the spin state above H_c are of great interest and currently under investigation.

[1] S. N. Bose, Z. Phys. **26**, 178 (1924).
[2] A. Einstein, Sitz. Ber. Preuss. Akad. Wiss. **1**, 3 (1925).
[3] F. London, Nature **141**, 643 (1938).
[4] M. H. Anderson, J. R. Ensher, M. R. Matthews, C. E. Wieman, and E. A. Cornell, Science **269**, 198 (1995).
[5] K. B. Davis, M.-O. Mewes, M. R. Andrews, N. J. van Druten, D. S. Durfee, D. M. Kurn, and W. Ketterle, Phys. Rev. Lett. **75**, 3969 (1995).
[6] H. Deng, H. Haug, and Y. Yamamoto, Rev. Mod. Phys. **82**, 1489 (2010).
[7] T. Byrnes, N. Y. Kim, and Y. Yamamoto, Nat. Phys. **10**, 803 (2014).
[8] T. M. Rice, Science **298**, 760 (2002).
[9] S. Sachdev, Nat. Phys. **4**, 173 (2008).
[10] A. Oosawa, M. Ishii, and H. Tanaka, J. Phys.: Condens. Matter **11**, 265 (1999).
[11] A. Oosawa, T. Takamasu, K. Tatani, H. Abe, N. Tsujii, O. Suzuki, H. Tanaka, G. Kido, and K. Kindo, Phys. Rev. B **66**, 104405 (2002).
[12] Ch. Rüegg, N. Cavadini, A. Furrer, H.-U. Güdel, K. Krämer, H. Mutka, A. Wildes, K. Habicht, and P. Vorderwisch, Nature (London) **423**, 62 (2003).
[13] M. Jaime, V. F. Correa, N. Harrison, C. D. Batista, N. Kawashima, Y. Kazuma, G. A. Jorge, R. Stern, I. Heinmaa, S. A. Zvyagin, Y. Sasago, and K. Uchinokura, Phys. Rev. Lett. **93**, 087203 (2004).
[14] S. E. Sebastian, N. Harrison, C. D. Batista, L. Balicas, P. A. Sharma, N. Kawashima, and I. R. Fisher, Nature **441**, 617 (2006).
[15] F. Yamada, T. Ono, H. Tanaka, G. Misguich, M. Oshikawa, and T. Sakakibara, J. Phys. Soc. Jpn. **77**, 013701 (2008).
[16] K. Goto, M. Fujisawa, T. Ono, H. Tanaka, and Y. Uwatoko, J. Phys. Soc. Jpn. **73**, 3254 (2004).
[17] A. Oosawa, M. Fujisawa, T. Osakabe, K. Kakurai, and H. Tanaka, J. Phys. Soc. Jpn. **72**, 1026 (2003).
[18] A. Oosawa, K. Kakurai, T. Osakabe, M. Nakamura, M. Takeda, and H. Tanaka, J. Phys. Soc. Jpn. **73**, 1446 (2004).

[19] Ch. Rüegg, A. Furrer, D. Sheptyakov, Th. Strässle, K. W. Krämer, H.-U. Güdel, and L. Mélési, Phys. Rev. Lett. **93**, 257201 (2004).
[20] Ch. Rüegg, B. Normand, M. Matsumoto, A. Furrer, D. F. McMorrow, K. W. Krämer, H.-U. Güdel, S. N. Gvasaliya, H. Mutka, and M. Boehm, Phys. Rev. Lett. **100**, 205701 (2008).
[21] K. Goto, M. Fujisawa, H. Tanaka, Y. Uwatoko, A. Oosawa, T. Osakabe, and K. Kakurai, J. Phys. Soc. Jpn. **75**, 064703 (2006).
[22] T. Nikuni, M. Oshikawa, A. Oosawa, and H. Tanaka, Phys. Rev. Lett. **84**, 5868 (2000).
[23] M. Matsumoto, B. Normand, T. M. Rice, and M. Sigrist, Phys. Rev. B **69**, 054423 (2004).
[24] O. Nohadani, S. Wessel, and S. Haas, Phys. Rev. B **72**, 024440 (2005).
[25] T. Giamarchi, Ch. Rüegg, and O. Tchernyshyov, Nat. Phys. **4**, 198 (2008).
[26] V. Zapf, M. Jaime, and C. D. Batista, Rev. Mod. Phys. **86**, 563 (2014).
[27] D. Pekker and C. M. Varma, Annu. Rev. Condens. Matter Phys. **6**, 269 (2015).
[28] V. L. Berezinskii, Sov. Phys. JETP **34**, 610 (1972).
[29] J. M. Kosterlitz and D. J. Thouless, J. Phys. C **5**, L124 (1972).
[30] J. M. Kosterlitz and D. J. Thouless, J. Phys. C **6**, 1181 (1973).
[31] U. Tutsch, B. Wolf, S. Wessel, L. Postulka, Y. Tsui, H. O. Jeschke, I. Opahle, T. Saha-Dasgupta, R. Valentí, A. Brühl, K. Remović-Langer, T. Kretz, H.-W. Lerner, M. Wagner, and M. Lang, Nat. Commun. **5**, 5169 (2014).
[32] R. Daou, F. Weickert, M. Nicklas, F. Steglich, A. Haase, and M. Doerr, Rev. Sci. Instrum. **81**, 033909 (2010).
[33] M. Jaime, R. Daou, S. A. Crooker, F. Weickert, Atsuko Uchida, A. E. Feiguin, C. D. Batista, H. A. Dabkowska, and B. D. Gaulin, PNAS **109**, 12404 (2012).
[34] P. Giannozzi, S. Baroni, N. Bonini, M. Calandra, R. Car, C. Cavazzoni, D. Ceresoli, G. L. Chiarotti, M. Cococcioni, I. Dabo, A. Dal Corso, S. Fabris, G. Fratesi, S.

de Gironcoli, R. Gebauer, U. Gerstmann, C. Gougoussis, A. Kokalj, M. Lazzeri, L. Martin-Samos, N. Marzari, F. Mauri, R. Mazzarello, S. Paolini, A. Pasquarello, L. Paulatto, C. Sbraccia, S. Scandolo, G. Sclauzero, A. P. Seitsonen, A. Smogunov, P. Umari and R. M. Wentzcovitch, J. Phys.: Condens. Matter **21**, 395502 (2009).

[35] K. F. Garrity, J. W. Bennett, K. M. Rabe, and D. Vanderbilt Comput. Mater. Sci. **81**, 446 (2014).

[36] H. J. Monkhorst and J. D. Pack, Phys. Rev. B **13**, 5188 (1976).

[37] J. P. Perdew, K. Burke, and M. Ernzerhof, Phys. Rev. Lett. **77**, 3865 (1996).

[38] M. Cococcioni and S. de Gironcoli, Phys. Rev. B **71**, 035105 (2005).

[39] H. J. Kulik, M. Cococcioni, D. A. Scherlis, and N. Marzari, Phys. Rev. Lett. **97**, 103001 (2006).

[40] N. Marzari and D. Vanderbilt, Phys. Rev. B **56**, 12847 (1997).

[41] A. A. Mostofi, J. R. Yates, Y.-S. Lee, I. Souza, D. Vanderbilt, and N. Marzari, Comput. Phys. Commun. **178**, 685 (2008).

[42] Note that, owing to the large (104 atoms) unit cell of $Ba_2CuSi_2O_6Cl_2$, the use of the supercell was not necessary in this case.

[43] G. Radtke, A. Saúl, H. A. Dabkowska, G. M. Luke, and G. A. Botton, Phys. Rev. Lett. **105**, 036401 (2010).

[44] A. Saúl and G. Radtke, Phys. Rev. Lett. **106**, 177203 (2011).

[45] A. Saúl and G. Radtke, Phys. Rev. B **89**, 104414 (2014).

[46] H. Tanaka, N. Kurita, M. Okada, E. Kunihiro, Y. Shirata, K. Fujii, H. Uekusa, A. Matsuo, K. Kindo, and H. Nojiri, J. Phys. Soc. Jpn. **83**, 103701 (2014).

[47] L. W. Finger, R. M. Hazen, and R. J. Hemley, Am. Mineral. **74**, 952 (1989).

[48] K. M. Sparta and G. Roth, Acta Crystallogr. B **60**, 491 (2004).

[49] Y. Sasago, K. Uchinokura, A. Zheludev, and G. Shirane, Phys. Rev. B **55**, 8357 (1997).

[50] E. C. Samulon, Z. Islam, S. E. Sebastian, P. B. Brooks, M. K. McCourt, Jr., J. Ilavsky, and I. R. Fisher, Phys. Rev. B **73**, 100407 (2006).

[51] Ch. Rüegg, D. F. McMorrow, B. Normand, H. M. Rønnow, S. E. Sebastian, I. R. Fisher, C. D. Batista, S. N. Gvasaliya, Ch. Niedermayer, and J. Stahn, Phys. Rev. Lett. **98**, 017202 (2007).

[52] F. Weickert, R. Kuchler, V. Zapf, M. Jaime, and A. Paduan-Filho, Phys. Rev. B **83**, 099901(E) (2011).

[53] I. Dzyaloshinsky, J. Phys. Chem. Solids **4**, 241 (1958).

[54] T. Moriya, Phys. Rev. **120**, 91 (1960).

[55] T. A. Kaplan, Z. Phys. B **49**, 313 (1983).

[56] L. Shekhtman, O. Entin-Wohlman, and A. Aharony, Phys. Rev. Lett. **69**, 836 (1992).

[57] A. Zheludev, S. Maslov, I. Tsukada, I. Zaliznyak, L. P. Regnault, T. Masuda, K. Uchinokura, R. Erwin, and G. Shirane, Phys. Rev. Lett. **81**, 5410 (1998).

[58] V. V. Mazurenko, M. V. Valentyuk, R. Stern, and A. A. Tsirlin, Phys. Rev. Lett. **112**, 107202 (2014).